Proceedings of the ASME 2012 Fluids Engineering Summer Meeting
FEDSM2012
July 8-12, 2012, Rio Grande, Puerto Rico, USA

FEDSM2012-72355

RELATIVE PERFORMANCE OF BODY-FITTED AND FICTITIOUS DOMAIN SIMULATIONS OF FLOW THROUGH POROUS MEDIA

Justin R. Finn
School of Mechanical Industrial
and Manufacturing Engineering
204 Rogers Hall
Oregon State University
Corvallis, Oregon 97331
Email: finnj@engr.oregonstate.edu

Sourabh V. Apte*
School of Mechanical Industrial
and Manufacturing Engineering
204 Rogers Hall, Room 308
Oregon State University
Corvallis, Oregon 97331
Email: sva@engr.oregonstate.edu

ABSTRACT

The relative performance of (i) a body-fitted unstructured grid Navier-Stokes solver [Moin and Apte, AIAA J. 2006], and (ii) a fictitious domain based finite-volume approach [Apte et al. JCP 2009] is examined for simulating flow through packed beds of spheres at moderate flow rates, $50 \lesssim Re \lesssim 1300$*. The latter employs non-body conforming Cartesian grids and enforces the no-slip conditions on the pore boundaries implicitly through a rigidity constraint force. At these flow rates, fluid inertia can result in complex steady and unsteady pore scale flow features that influence macro-scale properties. We examine the requirements on both methods to properly capture these features in both simple and complex arrangements of spheres. First, two prototypical test cases of flow through packed beds are studied thoroughly at a range of Reynolds numbers in the inertial flow regime. Next flow through a random packing of 51 spheres at* $Re = 1322$ *is simulated using both methods. The suitability of both approaches to the complex configurations observed in large randomly packed beds is discussed.*

INTRODUCTION

At moderate flow rates through porous media and packed beds, complex flow features such as helical vortices and jet stagnations have strong effects on macro-scale properties of broader interest including bulk mixing performance and net pressure drop across the medium. Many porous media processes occur at lower flow rates where such non-linear inertial effects may be modeled or neglected (ie. many geologic processes). However, higher flow rates in porous media also occur naturally, such as in river and stream beds, or may be a design feature, such as in packed bed chemical or nuclear reactors. In stream bed flows, inertial flow features can affect nutrient and temperature distributions [1, 2], while higher flow rates can be used to enhance reaction rates or heat transfer in packed bed reactors [3]. Rapidly increasing processing power has enabled highly resolved simulation (DNS/LES) to be a viable tool for understanding the flow physics governing these applications, including the pore scale flow dynamics. Porous media, however, present unique challenges to these techniques, mostly due to the complex solid/fluid interface. Nonetheless, successful simulations of these flows have been carried out for laboratory scale packings containing hundreds of spheres, most often using a body fitted (BF) grid combined with a finite volume approach [4–7]. While the body fitted approach has the ability to directly represent the fluid-solid interface, it is prone to significant meshing difficulties, and in general requires careful treatment of contacting spheres.

The mesh related pitfalls encountered in body fitted simulations can be avoided with a Cartesian grid immersed boundary (IB) [8, 9] or fictitious domain (FD) [10] approach. The differences between the two approaches are subtle, but important in the way that boundary conditions are enforced at the solid/fluid interface [11]. In general, immersed boundary techniques add

*Address all correspondence to this author.

a corrective term to the momentum equation corresponding to a solid-fluid interaction which satisfies the no-slip condition. In the fictitious domain (or distributed Lagrange multiplier) approach, the entire domain is treated as a single fluid (inclusive of solid regions), and the rigid motion of immersed solid objects is projected in one or more steps onto the flow field using Lagrangian force points located at the solid-fluid interface. In this work, the no slip condition at the pore-space surface is enforced through a rigidity constraint force, and the solid boundary is located with subgrid accuracy with Lagrangian marker points. These methods have been used extensively for investigations of fluidized beds, suspensions, and small arrangements of non-contacting fixed spheres [12], but have only been recently applied to fixed bed/porous media problems [13].

In this paper, we examine the performance of a fictitious domain approach for resolved simulation of flow through packed bed geometries, relative to the well established body fitted unstructured grid approach. The main goal is to demonstrate each method's strengths and weaknesses for porous media & packed bed applications. While the body fitted approach is able to directly represent the solid boundaries of the pores, it is prone to mesh quality issues in porous media. Cartesian grid methods, such as the fictitious domain approach used here are able to represent complex interfaces, but suffer from *interface smearing* on the order of the grid resolution. We first discuss the surface representation, and numerical solution procedure used by both methods. Next, grid independence and convergence are assessed for both methods with cases designed to test two difficult aspects of pore scale simulation in packed beds; accurate prediction of interstitial velocity profiles, and numerical representation of solid contact points without significant modification of the flow. To address the first issue, predictions of flow through a prototypical simple cubic packing are compared to experimentally measured interstitial velocity profiles by Suekane et al. [14]. To address the second issue, flow past a contacting pair of spheres at various angles of incidence is considered, and the influence of the contact point is evaluated. Finally, direct comparison of the methods are made for a random arrangement of 51 spheres at a pore Reynolds number of 1322. This case represents a realistic test of both methods applicability to engineering scale packed bed problems.

COMPUTATIONAL METHODS

Consider the Navier-Stokes equations for constant density, incompressible fluid motion:

$$\rho \left(\frac{\partial \mathbf{u}}{\partial t} + (\mathbf{u} \cdot \nabla) \mathbf{u} \right) = -\nabla p + \nabla \cdot \left[\mu \left(\nabla \mathbf{u} + (\nabla \mathbf{u})^T \right) \right] + \mathbf{f} \quad (1)$$

$$\nabla \cdot \mathbf{u} = 0 \quad (2)$$

where ρ is the density field, $\mathbf{u}$ the velocity vector, p the pressure, μ the fluid viscosity, $\mathbf{g}$ the gravitational acceleration, and $\mathbf{f}$ is an additional body force which is zero in the BF approach, and will be used to enforce rigidity within the solid phase in the FD approach. The BF and FD approaches to the solution of these equations are both implemented in a similar finite volume framework, and share several of the same basic techniques including fractional step and predictor-corrector schemes, and an algebraic multigrid (AMG) solver for the pressure Poisson equation [15]. The codes are parallelized using Message Passing Interface (MPI), allowing for larger scale simulations by distributing the required memory over many processors.

Regardless of the approach used, precise representation of the fluid-solid interface is critical to obtaining an accurate solution. Below, details are provided concerning the numerical representation of the porespace boundaries during simulation. For additional details regarding the numerical implementation and validation of each method, the reader is referred to [16] for the BF approach, and to [17, 18] for the FD approach.

BODY FITTED APPROACH

In the body fitted approach, the pore space is first discretized into unstructured tetrahedral control volumes. Arbitrarily shaped $CV's$ can be used, but in this work, all $CV's$ are tetrahedral, with a triangular mesh used to represent the solid surfaces of the spheres. Unstructured mesh generation for complex geometries is a non-trivial procedure in general, and in packed beds the process is complicated by sphere-to-sphere contact points, near which elements can become unmanageably small, have high aspect ratio, and be skewed. Several methods have been proposed to mitigate this problem. Most commonly, the spheres are created at reduced diameter, typically 98 or 99 percent, eliminating all contact points [5, 19, 20], and creating a small gap between spheres. A related approach first pursued by Guardo [4] is to create the spheres slightly larger than they actually are, so that they overlap. Magnico [7, 21] has used a structured grid approach where the surface representation is stair stepped due to a voxelized treatment of the solid boundaries. While the meshing overhead is low with this approach, an artificial surface roughness is imposed, even with significantly refined grids. The approach which is pursued here takes advantage of the fact that the fluid very close to the solid contact points tends to be more or less stagnant even at moderate Reynolds numbers. In light of this, Kuroki et al [22, 23] have proposed a *cylindrical bridge method*, whereby they do not change the diameter of the sphere, but rather unite two contacting spheres with a cylinder placed on the contact line as shown in FIG. 1. This technique has the potential to significantly reduce overall mesh size because the regions where small element sizes are required have been elimi-

nated. Nelson [24] extended this technique, and created a smooth fillet between the two contacting surfaces allowing for more continuity in the surface mesh and prismatic surface layers.

The bulk behavior of porous media flows is strongly affected by porosity, so it is important that the cylinder bridges do not add significant solid volume to the porespace. The overall *increase in solid volume* due to the artificial bridges can be shown to be $V_b = N_b \left[2\pi R_b^2 \left(R_{sp} - \sqrt{R_{sp}^2 - R_b^2} \right) \right]$, where N_b is the total number of bridges required. In this work, the bridge radius is chosen to be $R_b \leq 0.25 R_{sp}$, so the volume of a single cylinder bridge is $V_b = 0.0011\ V_s$. Thus, even for packings with large coordination numbers, we can expect the total solid volume to increase by less than 1% (and only in the mostly stagnant contact regions). By comparison, the more common technique of shrinking the spheres to 99% of their original size will decrease the solid volume (everywhere) by roughly 3%.

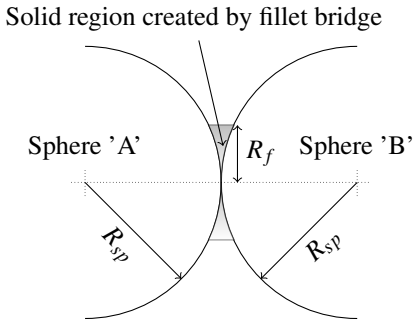

FIGURE 1: SCHEMATIC OF THE CYLINDER BRIDGE CREATED BETWEEN TWO CONTACTING SPHERES.

It quickly becomes challenging and time consuming to generate this type of geometry and mesh for more than a few spheres using the GUI of a typical mesh generation package because of the large number of geometric entities and high surface area-to-volume ratio. In light of this, a parameterized and automated approach has been developed that takes advantage of the commercial meshing package Pointwise's® full TCL-TK programmability. All sphere-sphere or sphere-boundary contact points are bridged, then trimmed and joined into a single watertight model. Once the solid geometry is assembled, a triangular surface mesh is generated on all solid surfaces. The local surface mesh spacing, Δ is chosen so that spacing of the surface mesh is constant on the sphere pack surface. Finally the volume is meshed with tetrahedral CV's whose size matches Δ near the surface, and coarsens slightly far from the solid boundaries. An example of the cylinder bridge geometry and surface mesh is shown in the lower half of FIG. 2 for a simple 2-sphere system. This meshing tool is robust and can handle arbitrary random or arranged packings of spheres contained in box or tube geometries. It has been used to generate meshes with over 30 million *CV* and for geometries containing over 500 spheres.

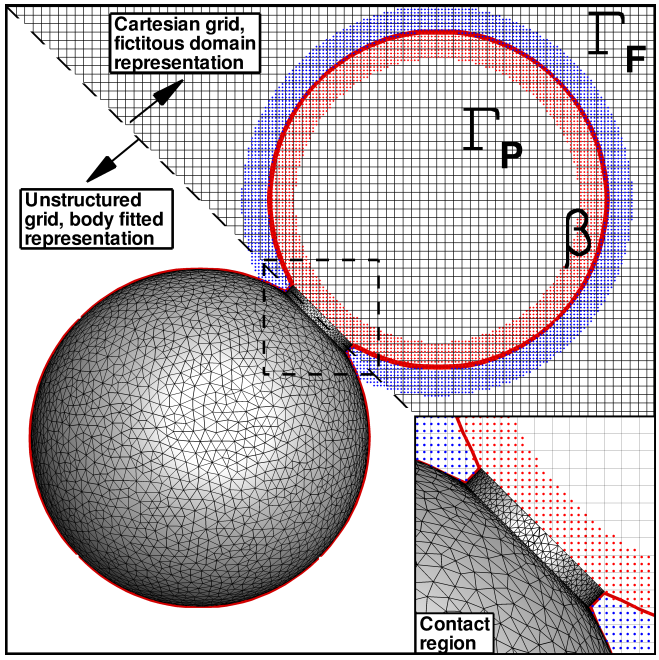

FIGURE 2: COMPARISON OF DISCRETE SURFACE REPRESENTATION SCHEMES USED IN THE BODY FITTED AND FICTITIOUS DOMAIN APPROACHES.

FICTITIOUS DOMAIN APPROACH

The computations carried out with the FD approach utilize a hybrid Lagrangian-Eulerian (HLE) formulation for representation of arbitrarily shaped immersed solid objects and is not limited to the spherical objects used here. Although we consider only fixed beds, the fictitious domain approach [10, 17, 25] also allows accurate representation of moving boundaries embedded in a fluid flow. Let Γ be the the entire computational domain which includes both the fluid (Γ_F) and the solid particle (Γ_P) domains shown in upper half of FIG. 2. Let the fluid boundary not shared with the particle be denoted by $\mathscr{B}$ and have a Dirichlet condition (generalization of boundary conditions is possible). The basis of a fictitious-domain approach [10] is to extend the Navier-Stokes equations for fluid motion over the entire domain Γ inclusive of immersed solids. The natural choice for these fixed bed problems is to assume that the immersed solid region, Γ_P, is filled with the same Newtonian *fluid* with density (ρ) and viscosity (μ) as Γ_F. Both the real and fictitious fluid regions will be

assumed as incompressible and thus equations 1 and 2 apply everywhere in the domain. In addition, as the immersed solids are assumed rigid, the motion of the material inside Γ_P is constrained to rigid body motion. Several ways of obtaining the rigidity constraint have been proposed [10, 25, 26]. We follow the formulation developed by Patankar [25] and described in detail by Apte et al. [17]. A brief description is given here for completeness. The FD approach utilizes, non body conformal Cartesian grids, greatly simplifying the meshing process. The solid fluid interface, $\mathscr{B}$ is located on the grid with subgrid scale marker points as shown in the top half of FIG. 2. These marker points carry a color function indicating the relative location of the interface, and remain fixed during the simulations.

In order to enforce that the material inside the immersed solid moves in a rigid fashion, a rigidity constraint is required that leads to a non-zero forcing function $\mathbf{f}$. Inside the particle region, the rigid body motion, $\mathbf{u}^{RBM}$ implies vanishing deformation rate tensor:

$$\left.\begin{array}{l} \frac{1}{2}\left(\nabla\mathbf{u}+(\nabla\mathbf{u})^T\right)=\mathbf{D}[\mathbf{u}]=0, \\ \Rightarrow \mathbf{u}=\mathbf{u}^{RBM}=\mathbf{U}+\Omega\times\mathbf{r} \end{array}\right\} \text{ in } \Gamma_P, \tag{3}$$

where $\mathbf{U}$ and Ω are the translation and angular velocities of the object and $\mathbf{r}$ is the position vector of a point inside the object from its centroid. For the fixed bed problems considered here, $\mathbf{u}^{RBM}$ is always zero. The vanishing deformation rate tensor for rigidity constraint automatically ensures the divergence free, incompressibility constraint inside the particle region. The incompressibility constraint gives rise to the scalar field (the pressure, p) in a fluid. Similarly, the tensor constraint $\mathbf{D}[\mathbf{u}]=0$ for rigid motion gives rise to a tensor field inside the particle region [26]. Distributed Lagrange multipliers (DLM)-based approaches have been proposed to solve for the rigid body motion and impose the rigidity constraint which requires an iterative solution strategy. Patankar [27] proposed an approach that provides the rigidity constraint explicitly, thus reducing the computational cost significantly. Noting that the tensorial rigidity constraint can be reformulated to give:

$$\nabla\cdot(\mathbf{D}[\mathbf{u}])=0 \; in \; \Gamma_P \tag{4}$$

$$\mathbf{D}[\mathbf{u}]=0 \; on \; solid/fluid \; interface \tag{5}$$

A fractional-step algorithm can be devised to solve the fictitious domain problem [17, 25, 28]. Knowing solution at time level t^n the goal is to find $\mathbf{u}$ at time t^{n+1}.

1. In the first step, the rigidity constraint force $\mathbf{f}$ in equation 1 is set to zero and the equation together with the incompressibility constraint (equation 3) is solved by standard fractional-step schemes over the entire domain. Accordingly, a pressure Poisson equation is derived and used to project the velocity field onto an incompressible solution. The obtained velocity field is denoted as $\mathbf{u}^{n+1}$ inside the fluid domain and $\hat{\mathbf{u}}$ inside the rigid object.
2. To solve for $\mathbf{u}^{n+1}$ inside the particle region we require $\mathbf{f}$. The constraint on the deformation rate tensor given by equation 3, along with the no-slip specification at the solid-fluid interface can be reformulated to obtain:

$$\nabla\cdot\left(\mathbf{D}[\mathbf{u}^{n+1}]\right)=\nabla\cdot\left(\mathbf{D}\left[\hat{\mathbf{u}}+\frac{\mathbf{f}\Delta t}{\rho}\right]\right)=0; \tag{6}$$

$$\mathbf{D}[\mathbf{u}^{n+1}]\cdot\mathbf{n}=\mathbf{D}\left[\hat{\mathbf{u}}+\frac{\mathbf{f}\Delta t}{\rho}\right]\cdot\mathbf{n}=0. \tag{7}$$

   The velocity field, $\mathbf{u}^{n+1}$, is zero for fixed beds. Thus $\hat{\mathbf{u}}$ is split into a rigid body motion ($\mathbf{u}^{RBM}=\mathbf{U}+\Omega\times\mathbf{r}=0$) and residual non-rigid motion ($\mathbf{u}'$). The above formulation can be easily generalized to particles with *specified motion* by directly setting $\mathbf{u}^{RBM}$ to the specified velocity.
3. The rigidity constraint force is then simply obtained as $\mathbf{f}=\rho(\mathbf{u}^{RBM}-\hat{\mathbf{u}})/\Delta t$. This sets $\mathbf{u}^{n+1}=\mathbf{u}^{RBM}$ in the particle domain. Note that the rigidity constraint is non-zero only inside the particle domain and zero everywhere else. This constraint is then imposed in a third fractional step.

The utility of the Lagrangian marker points (cf FIG. 2) is in locating the solid/fluid interface with subgrid scale resolution in the above steps. A quantity can be defined and calculated at the marker points (for example $\mathbf{f}$) and then be projected onto the Eulerian grid, or vice-versa, using accurate interpolation kernels [17]. This allows for the no-slip condition at the solid boundary to be enforced with sub-grid precision.

In practice, because the no-slip condition at the boundary of the porespace is enforced through such indirect interpolations, the precision of the boundary location is directly linked to the grid resolution. This is especially true near regions of sharp boundary curvature such as sphere to sphere contact points. This is illustrated in the top half of FIG. 2 where the solid line denotes the fictitious domain solid-fluid interface. Even with subgrid marker points, the high curvature contact region appears as a *bridge* similar to the one obtained in the body fitted meshing procedure.

VALIDATION CASES

Two basic test cases are studied thoroughly to validate and compare the performance of the two methods for fixed bed problems. First, we compare predicted velocity profiles to those measured experimentally by Suekane et al. [14] in a simple cubic packing section. Next, to test the effect of the cylinder bridge meshing model in the BF approach and the embedded interface

in the FD approach, we simulate flow past a contacting pair of spheres for a variety of incidence angles and Reynolds numbers.

THE "SUEKANE" CASE

We first compare our numeric prediction of interstitial flow velocity to the experimental measurements of Suekane et al. [14]. They used MRI techniques to obtain detailed, three dimensional measurements of the flow velocity in a porous channel resembling a section of a simple cubic lattice shown in FIG. 3. To our knowledge, this is one of the only studies where detailed interstitial velocity profiles have been obtained in a porous like geometry, and has served as a validation for several other studies including [13, 29]. The flow domain is shown in figure 3. Flow enters from the bottom of a square section, with side length equal to $28mm$. Six layers of quarter spheres having diameter $D_s = 28mm$ are stacked one on top of another in an ordered arrangement. The domain is discretized using unstructured, tetrahedral meshes for the BF approach and regular Cartesian grids for the BF approach. The spheres were created at their exact size, and a small area is removed from the unstructured meshes near the contact points as described previously. Four meshes were generated for each method with the same mean spacing, D_{sp}/Δ everywhere and are summarized in TAB. 1. The BF meshes use $D_{sp}/\Delta = 7,\ 14,\ 28,\ 56$, and the FD meshes use $D_{sp}/\Delta = 10,\ 20,\ 30,\ 40$. The flow enters from the bottom of the domain at a constant flow rate, Q, defined by the Reynolds number, $Re = \rho V_{mean} D_s/\mu$ where $V_{mean} = Q/A\varepsilon$, A is the inlet area, and $\varepsilon = 0.52$ is the porosity for this simple cubic lattice. For comparison to the experiments, flow through the pore space is simulated at $Re = 105.57$, the experimental Reynolds number with the lowest experimental uncertainty (as noted by [29]), and representative of the flow rates studied later in this work. The flow is started from rest and simulated for $\overline{T} = tV_{mean}/D_{sp} = 10$ non dimensional flow through times. Fluid interstitial velocity profiles are extracted at the end of the simulation in the $Z = 0mm$ plane and the $Z = 14mm$ plane as shown in FIG. 3.

The $Z = 0$ measurement corresponds to the location of data collected in the experiments, the middle of the 5th pore where flow area is maximized. We plot the streamwise velocity as a function of position along the X axis in figure 4a-b alongside the experimental data of [14]. As the mesh is refined, the solution of both methods approach the experimental values. At this Reynolds number, the significant flow inertia gives rise to a strong jet through the center of the pore ($|X/r| \lesssim 0.3$), and symmetric backflow regions close to the walls ($|X/r| \approx 0.7$). The computational results show that these features can be sufficiently resolved with grid resolution of $D_{sp}/\Delta = 28$ using the body fitted approach, or $D_{sp}/\Delta = 20$ using the FD approach. Also, the similar solutions obtained using grids at this resolution or finer indicate grid convergence at this Re. We also check the computed velocity profiles in the $Z = 14$ plane, shown in figure 4c-d.

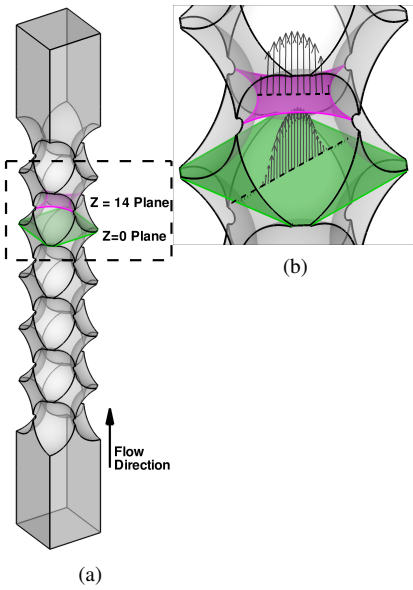

FIGURE 3: SETUP OF THE "SUEKANE TEST CASE"

TABLE 1: GRIDS USED BY BOTH APPROACHES AND THE REQUIRED SIMULATION TIME FOR $\overline{T} = tV_{mean}/D_{sp} = 10$ FLOW THROUGH TIMES IN THE SUEKANE GEOMETRY AT $Re = 105$

Body Fitted				
D_{sp}/Δ	7	14	28	56
N_{cv}	32k	110k,	490k	2.2m
Fictitious Domain				
D_{sp}/Δ	10	20	20	40
N_{cv}	10k	77k,	258k	612k

At this location, the flow is confined to the throat of the pore, resulting in a stronger jet than at $Z = 0$, and there will be less grid points available to resolve the strong gradients due to flow inertia. We see that the strength of the jet is significantly underpredicted by the coarse grids, while $D_{sp}/\Delta = 28$ and $D_{sp}/\Delta = 20$ are again required to obtain grid convergence with the BF and FD methods respectively.

FLOW PAST A CONTACTING PAIR

Flow past a contacting pair of spheres in a confined channel is chosen as a second assessment of grid convergence and also as a way to isolate the effect of sphere to sphere contact regions on both methods. The flow configuration is shown in FIG. 5, and

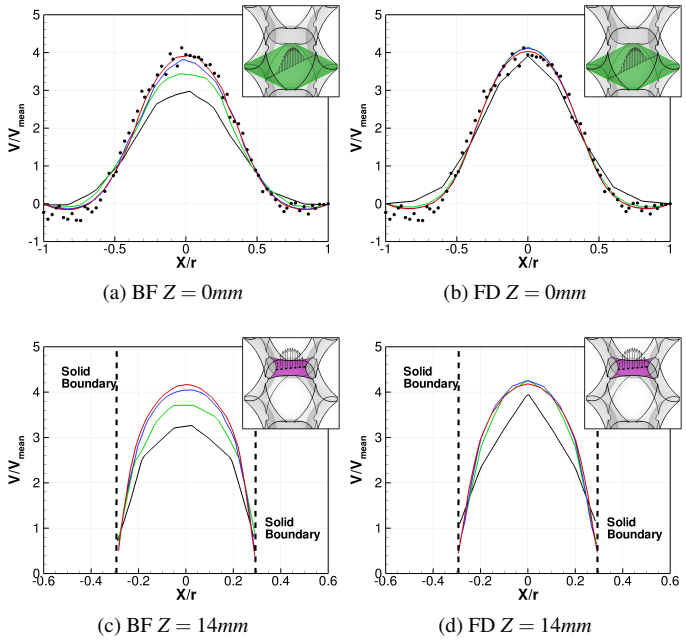

(a) BF $Z = 0mm$ (b) FD $Z = 0mm$

(c) BF $Z = 14mm$ (d) FD $Z = 14mm$

FIGURE 4: GRID CONVERGENCE OF SIMULATED INTERSTITIAL VELOCITY PROFILES WITH MESH REFINEMENT FOR TWO PLANES IN THE SUEKANE GEOMETRY (a,b) THE $Z = 0$ PLANE, (c,d) THE $Z = 14$ PLANE, DASHED LINES SHOW NO-SLIP BOUNDARY LOCATION. GRID RESOLUTION FOR BF/FD METHODS: (—) $D_{sp}/\Delta = 7/10$, (—) $D_{sp}/\Delta = 14/20$, (—) $D_{sp}/\Delta = 28/30$, (—) $D_{sp}/\Delta = 56/40$, ● EXPERIMENTAL RESULTS OF SUEKANE ET AL. 2003

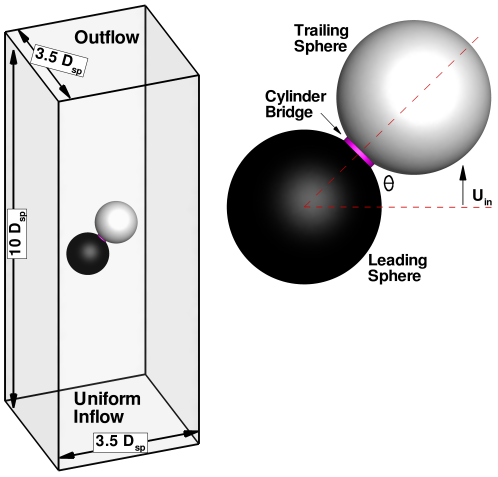

FIGURE 5: CONFIGURATION FOR SIMULATION OF FLOW PAST THE CONTACTING PAIR.

TABLE 2: SIMULATION PARAMETERS RELEVANT TO THE SETUP OF THE CONTACTING PAIR STUDY.

Re	50, 75, 100, 125, 150, 175
θ^o	0, 15, 30, 45, 60, 75, 90
L_x, L_y, L_z	$3.5D_{sp}$, $3.5D_{sp}$, $10.0D_{sp}$
D_{sp}/Δ (BF)	14, 20, 28, 40, 56
D_{sp}/Δ (FD)	15, 20, 25, 30, 35, 40

relevant simulation parameters are summarized in TAB. 2. The spheres are located such that their contact point always lies at the origin, $(X,Y,Z) = 0$. Uniform flow enters from a square cross section, $3.5D_{sp} \times 3.5D_{sp}$ at $Z = -5D_{sp}$. A convective outflow boundary is located downstream of the contact at $Z = +5D_{sp}$. A no-slip condition is enforced on the channel walls. The spheres are rotated around the Y axis by the angle of incidence θ so that the leading and trailing sphere centers have the coordinates

$$(X_l,\, Y_l,\, Z_l) = \left(0,\; -\frac{D_{sp}}{2}\sin(\theta),\; -\frac{D_{sp}}{2}\cos(\theta)\right)$$
$$(X_t,\, Y_t,\, Z_t) = \left(0,\; \frac{D_{sp}}{2}\sin(\theta),\; \frac{D_{sp}}{2}\cos(\theta)\right)$$

The value of θ is varied from 0^o to 90^o in increments of 15^o in order to fully sample the range of orientations found in realistic packed beds. The uniform inflow velocity is assigned so the Reynolds number, defined $Re = \rho U_{in} D_{sp}/\mu$ is between 50 and 175, in intervals of 25. For unbounded flow over a single sphere, a transition to unsteadiness is expected around $Re = 300$ [30], and further simulations will be completed in the future with this case to show grid convergence properties in the unsteady flow regime. In all cases the flow is started from rest, and allowed to develop for $\bar{T} = tU_{in}/D_{sp} = 30$ flow through times. Mean grid spacing on the surface and in the vicinity of the pair is in the range $14 \leq D_{sp}/\Delta \leq 56$ for the BF approach and $15 \leq D_{sp}/\Delta \leq 40$ for the FD approach. Since the goal of this study is to determine the effect of near sphere grid resolution, the grids are allowed to coarsen far away from the pair near the inflow and outflow regions. At a distance of $1.5D_{sp}$ away from the contact line, the grid spacing is never greater than twice the surface spacing.

We first confirm that our flow is steady by monitoring the drag force signal on the surface of the spheres and verifying that no oscillations are present for the entire range of present conditions. For the confined cases studied here, we see the development of complex, yet steady flow features as shown in FIG. 6. Here, we show select stream-ribbons for $\theta = 0^o$, 30^o, 60^o,and $\theta = 90^o$ along with pressure contours in the $X = 0$ plane. At

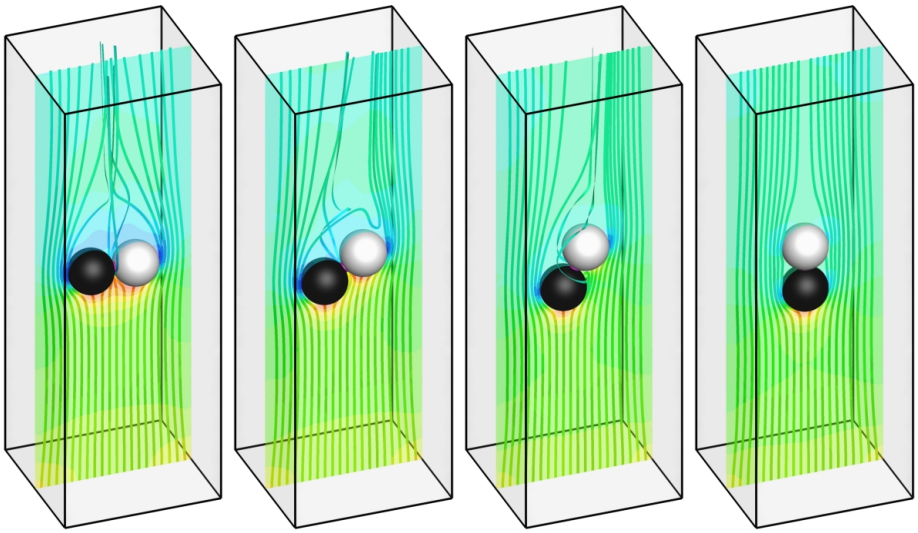

(a) $\theta = 0$ (b) $\theta = 30$ (c) $\theta = 60$ (d) $\theta = 90$

FIGURE 6: STREAM RIBBON VISUALIZATION OF FLOW AROUND THE PAIR OF SPHERES AT $RE = 175$ AND SELECT ANGLES OF INCIDENCE. PRESSURE CONTOURS ARE SHOWN IN THE $X = 0$ PLANE; RED INDICATES HIGH PRESSURE, BLUE INDICATES LOW PRESSURE.

$\theta = 0$, the flow stagnates evenly on both spheres and the contact point, generating a large symmetric recirculation bubble. As the angle of incidence is increased to 30^o and 60^o, the recirculation bubble bends away from the leading sphere and towards the trailing sphere and the flow is no longer symmetric about the contact line. At $\theta = 60^o$ there is a noticeable decrease in stagnation pressure on the trailing sphere, suggesting a drafting effect is present. At $\theta = 90^0$, symmetry is regained as the two-sphere body becomes streamlined, and the contact point is completely hidden from the flow by the leading sphere.

The drag coefficient over the entire connected body, C_D^{total} is monitored at all values of Re and θ considered in TAB. 2.

$$C_D^{total} = \frac{F_z^L + F_z^T + F_z^F}{\frac{1}{8}\rho U_{in}^2 \pi D_{sp}^2} \tag{8}$$

In the BF approach, we can isolate the force on the leading sphere, F_z^L, the trailing sphere, F_z^T, and the bridge F_z^B by computing directly the surface integral of viscous and pressure forces on each of the solid boundary zones separately. In the FD approach, we compute the force balance on a control volume drawn around the entire connected body to compute the total force acting on the two immersed spheres. The results of this calculation at select angles computed by both methods is shown in FIG. 7 for the finest grid solution (FD/BF $D_{sp}/\Delta = 56/40$). Both methods predict the same trend in C_D^{total} over the range of Re explored, although the FD approach consistently under predicts the value relative to the BF approach by about 3-7%. Since the trends predicted by both approaches are identical, part of this may be due to the difference in the drag calculation method.

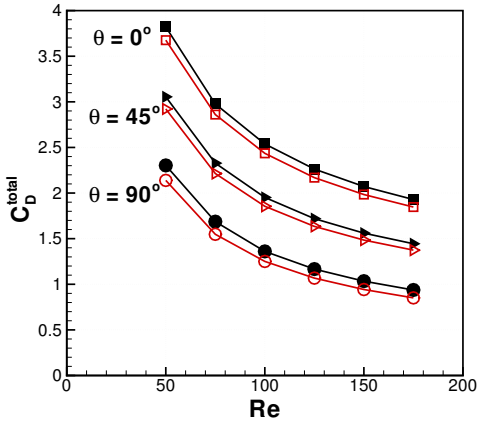

FIGURE 7: TOTAL DRAG COEFFICIENT OF THE CONTACTING PAIR COMPUTED USING THE BF APPROACH (CLOSED SYMBOLS) AND THE FD APPROACH(OPEN SYMBOLS) FOR ALL REYNOLDS NUMBERS AT $\theta = 0^o$, 45^o, 90^o ANGLE OF INCIDENCE

The grid convergence of both methods is assessed by examining the computed value of C_D^{total} on all grids at $Re = 175$, $\theta =$

45^o as shown in FIG. 8a. The results show both methods converging to a constant value with increasing grid refinement. The FD method obtains approaches a converged solution at a coarser resolution of $D_{sp}/\Delta \approx 30$ compared to the BF solution which requires $D_{sp}/\Delta \approx 40$. This is a stricter requirement for convergence than in the *Suekane case*, perhaps because of the integral measure being used. A Richardson extrapolation of both trends is used to estimate the solution at infinite grid resolution ($\Delta \to 0$), and is indicated by the dashed lines in FIG 8a. Using this as a reference solution, we plot the relative error in C_D for each grid in FIG. 8b. Despite our lack of an analytic solution or experimental data, the logarithmic decrease in this metric suggests between first and second order accuracy of the computations. The order of accuracy in computing this metric is noticeably better using the FD approach (close to second order). Because the same solvers, and discretization schemes are used by both methods, we can attribute the lower degree of accuracy to the quality of the body fitted grids relative to the regular Cartesian grids used by the fictitious domain approach.

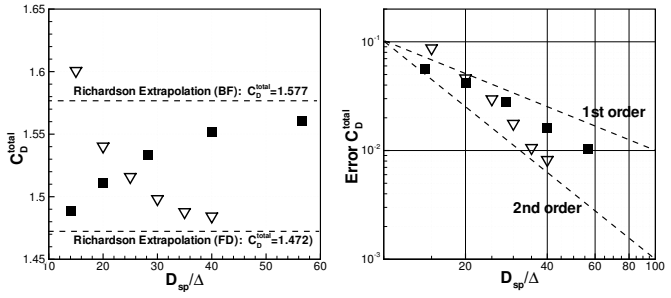

FIGURE 8: GRID CONVERGENCE OF THE TOTAL DRAG COEFFICIENT OF THE PAIR AT $\theta = 45^o$, $Re = 150$. ERROR IS MEASURED AS THE DEVIATION FROM THE FINE GRID SOLUTION FOR EACH APPROACH. ■ BF APPROACH, ▽ FD APPROACH.

Next, the effect of the contact point is considered in the BF results using the finest grid solution ($D_{SP}/\Delta = 56$). In FIG. 9 the ratio of drag force on the trailing and leading sphere (FIG. 9a), as well as the ratio of drag force on the bridge to the leading sphere is plotted (FIG. 9b). This demonstrates the increased drafting ability of the trailing sphere at increased θ or increased Re as would be expected. For all combinations of Re and θ, the contribution of the cylinder bridge to the total drag of the pair is less than 1% of the leading spheres contribution. This ratio is maximized at all Re for $\theta = 0$, and decreases as the cylinder surface is rotated out of the stagnation region. Roughly extrapolating, the cylinder bridge drag will be 1% of the leading sphere drag at $\theta = 0$ for $Re \approx 600$, a much large Reynolds number than the scope of this test. However, bridged contact regions may affect the transient dynamics of unsteady and turbulent flows at higher Re, and a similar type of sensitivity test would be needed before extending the present methods to those regimes.

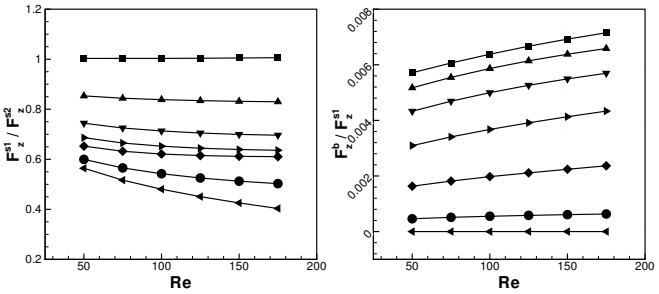

(a) TRAILING SPHERE (b) CYLINDER BRIDGE

FIGURE 9: RATIO OF DRAG FORCE ON (a) THE TRAILING SPHERE F_z^{s2}/F_z^{s1} (b) THE BRIDGE F_z^b/F_z^{s1}, AS A FUNCTION OF Re FOR ALL VALUES OF θ TESTED. ■ $\theta = 0^o$, ▲ $\theta = 15^o$, ▼ $\theta = 30^o$,► $\theta = 45^o$, ♦ $\theta = 60^o$,● $\theta = 75^o$,◄ $\theta = 90^o$.

To verify that the FD representation of the surface is consistent with the BF representation, especially near the contact points, the velocity profile in the near wake behind the cylinder bridge is plotted in FIG. 10 at $Re = 175$, $\theta = 0$. Despite the close proximity of the profiles to the solid-fluid interface, the wake profiles are predicted to be nearly identical by both approaches. This provides confidence in the ability of the FD approach to accurately handle the contacting spherical bodies encountered in realistic fixed bed geometries.

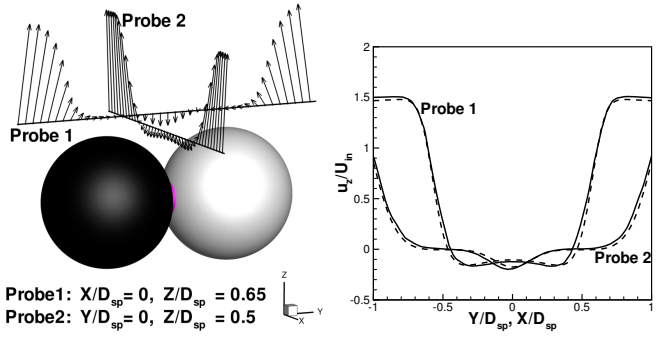

(a) PROBE LOCATION (b) STREAMWISE VELOCITY

FIGURE 10: VELOCITY PROFILES BEHIND THE CONTACTING PAIR AT $Re = 175$, $\theta = 0^o$. (a) SHOWS THE PROBE LOCATIONS (b) STREAMWISE VELOCITY PROFILE (—)BF APPROACH, (- - -)FD APPROACH.

FLOW THROUGH A RANDOMLY PACKED BED

We now turn to a more realistic scenario of flow through a randomly packed bed of spheres. The packing is composed of 51 spheres packed randomly in a box with sides $L_x = L_y = L_z = 4D_{sp}$ and is shown in the left side of FIG. 11. A *ballistic deposition* algorithm was used to pack the box, similar to the method employed by [5] resulting in a mean volume fraction $\varepsilon = 0.58$ The flow is driven in the positive Z direction by a constant inflow velocity boundary located $3D_{sp}$ upstream of the packing so that the Reynolds number for the flow is $Re = \frac{\rho U_{in} * D_{sp}}{\mu} \cdot \frac{1}{1-\varepsilon} = 1322$, where U_{in} is the bulk or superficial flow velocity. A convective outlet condition is located $3D_{sp}$ downstream of the packing.

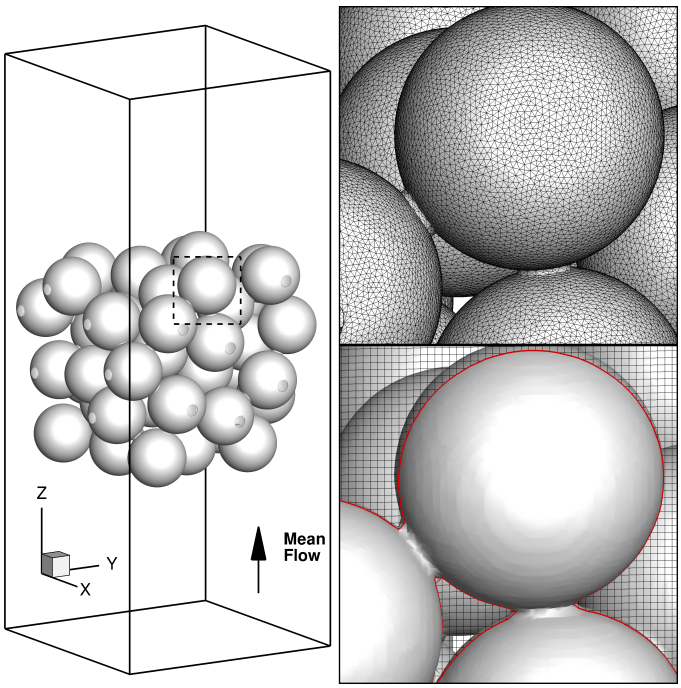

FIGURE 11: THE GEOMETRY CONSIDERED FOR FLOW THROUGH A RANDOM PACKING. THE VIEWS ON THE RIGHT COMPARE THE MESHES AND SURFACE REPRESENTATIONS OBTAINED USING THE BF AND FD APPROACHES.

Two meshes were created to simulate flow through this packing using the BF and FD approaches. For the BF approach, a body fitted mesh of tetrahedral elements was used with a mean spacing of $D_{sp}/\Delta = 80$ on the sphere surfaces. The unstructured mesh is allowed to expand slightly away from the sphere surfaces, but the mean spacing in the porespace does not exceed $D_{sp}/\Delta = 40$. For the FD approach, a regular Cartesian grid was used with a spacing of $D_{sp}/\Delta = 38$ everywhere in the porespace. The mesh was stretched toward the inflow and outflow boundaries. The tetrahedral mesh for the BF approach contains a total of 13.6 million CV, while the Cartesian grid for the FD approach contains 4.8 million CV. The right side of figure 11 illustrates the surface representation obtained by the two approaches. At these grid refinement levels, both representations are high quality, and seem to be quite close to one another.

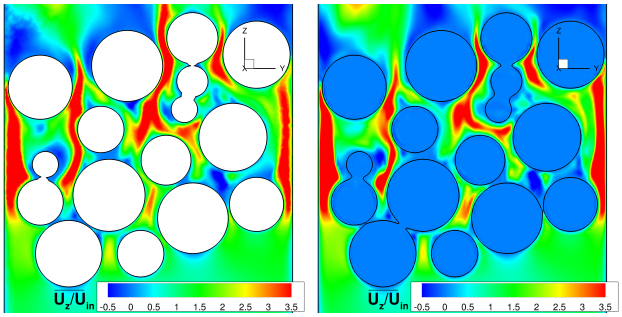

FIGURE 12: CONTOUR PLOT OF NORMALIZED TIME AVERAGED STREAMWISE VELOCITY IN A PLANE LOCATED AT $X = 2$.

The flow was started from rest and allowed to develop to for $\overline{T}U_{in}/D_{sp} = 21$ non-dimensional flow through times. At this Reynolds number, the flow in the porespace is fully turbulent. The time averaged streamwise velocity field is plotted for a slice through the center of the porespace in FIG. 12. This mean flow is complex, and marked by a variety of behavior including high velocity channels, and low velocity wake regions. While there are some differences that can be detected with the eye, the main features of the flow are consistent between the two methods. The swirling strength criteria [31], λ_{ci} is used to detect pore-scale vortical structures in the instantaneous flow fields. Three dimensional iso-surfaces of this criteria obtained with the FD solution is shown in FIG. 13. The entire porespace is filled with worm-like vortical structures reminiscent of those seen in isotropic box turbulence [32]. This demonstrates the capability of the FD approach for higher Reynolds number flows.

Due to the regularity of the grid, the FD approach is able to use a larger timestep while still respecting the same CFL condition as the BF approach. This leads to the potential for significant savings in CPU time for large simulations such as this one. For example, although the FD grid spacing is twice as large as the BF grid spacing, it is able to run with a timestep almost 10 times as large.

CONCLUSIONS

The relative performance of a fictitious-domain approach compared to a body fitted approach has been assessed for sim-

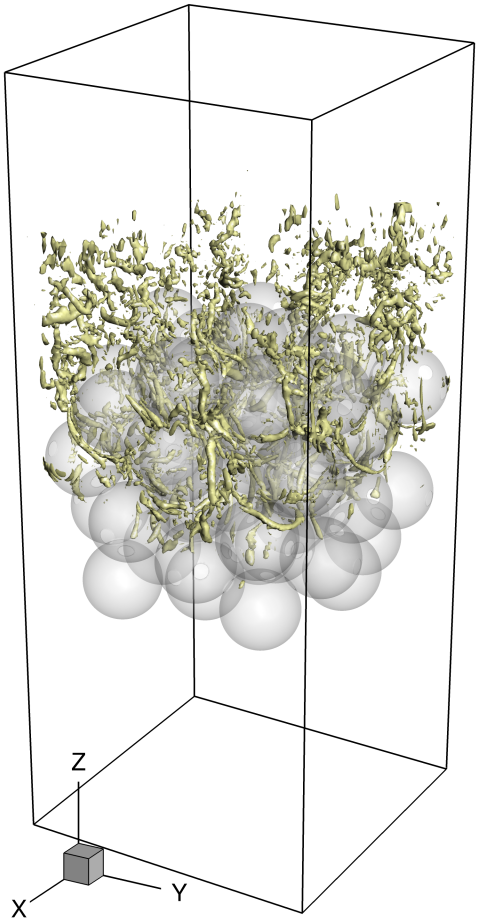

FIGURE 13: VORTICAL STRUCTURES DETECTED WITH THE FICTITIOUS DOMAIN APPROACH. ISOSURFACE OF $\lambda_{ci} = 13$ IS SHOWN.

ulation of flow through packed beds of spheres. The body-fitted approach utilizes a cylinder bridge model during mesh generation to avoid troublesome sphere to sphere contact points. This mesh generation approach avoids major modification of the solid geometry and removes areas where small elements are required. The main advantage of the fictitious domain approach for fixed bed and porous media problems is that it can use regular Cartesian grids, and avoids unstructured mesh generation all together. The solid-fluid interface is accurately represented using Lagrangian marker points with subgrid resolution, and a rigidity constraint within the solid bodies is imposed to enforce the no-slip.

The two approaches have been applied to two prototypical problems to benchmark their performance. For the moderate Reynolds numbers considered, the fictitious domain approach outperforms the body fitted approach in terms of grid spacing required for grid convergent solutions, most likely due to the quality of the regular Cartesian grids. The two approaches have also been applied to a more practical case of turbulent flow at $Re = 1322$ through a random packing of 51 spheres. Mean velocity fields predicted by both methods are in agreement, and the level of detail provided by both methods allows for the extraction and visualization of complex pore-scale vortical structures.

ACKNOWLEDGMENT

This work was supported by the National Science Foundation (Project #0933857: *Inertial Effects in Flow Through Porous Media*). The simulations of flow through the randomly packed bed were performed on the Lonestar supercomputer at the Texas Advanced Computing Center.

REFERENCES

[1] Cardenas, M., and Wilson, J., 2007. "Dunes, turbulent eddies, and interfacial exchange with permeable sediments". *Water Resour. Res,* ***43***(8), p. W08412.

[2] Dagan, G., 1984. "Solute transport in heterogeneous porous formations". *Journal of Fluid Mechanics,* ***145***, pp. 151–77.

[3] Andrigo, P., Bagatin, R., and Pagani, G., 1999. "Fixed bed reactors". *Catalysis today,* ***52***(2-3), pp. 197–221.

[4] Guardo, A., Coussirat, M., Recasens, F., Larrayoz, M., and Escaler, X., 2006. "CFD study on particle-to-fluid heat transfer in fixed bed reactors: Convective heat transfer at low and high pressure". *Chemical Engineering Science,* ***61***(13), pp. 4341–4353.

[5] Atmakidis, T., and Kenig, E., 2009. "CFD-based analysis of the wall effect on the pressure drop in packed beds with moderate tube/particle diameter ratios in the laminar flow regime". *Chemical Engineering Journal*.

[6] Dixon, A., Nijemeisland, M., and Stitt, E., 2006. "Packed tubular reactor modeling and catalyst design using computational fluid dynamics". *Computational Fluid Dynamics*, p. 307.

[7] Magnico, P., 2009. "Pore-scale simulations of unsteady flow and heat transfer in tubular fixed beds". *AIChE Journal,* ***55***(4), pp. 849–867.

[8] Mittal, R., and Iaccarino, G., 2005. "Immersed boundary methods". *Annu. Rev. Fluid Mech.,* ***37***, pp. 239–261.

[9] Peskin, C., 2003. "The immersed boundary method". *Acta Numerica,* ***11***, pp. 479–517.

[10] Glowinski, R., Pan, T., Hesla, T., Joseph, D., and Periaux, J., 2001. "A fictitious domain approach to the direct numerical simulation of incompressible viscous flow past moving rigid bodies: application to particulate flow". *Journal of Computational Physics,* ***169***(2), pp. 363–426.

[11] Taira, K., and Colonius, T., 2007. "The immersed boundary

method: a projection approach". *Journal of Computational Physics,* ***225***(2), pp. 2118–2137.

[12] Yu, Z., Shao, X., and Wachs, A., 2006. "A fictitious domain method for particulate flows with heat transfer". *Journal of Computational Physics,* ***217***(2), pp. 424–452.

[13] Ovaysi, S., and Piri, M., 2010. "Direct pore-level modeling of incompressible fluid flow in porous media". *Journal of Computational Physics,* ***229***(19), pp. 7456–7476.

[14] Suekane, T., Yokouchi, Y., and Hirai, S., 2003. "Inertial flow structures in a simple-packed bed of spheres". *AIChE Journal,* ***49***(1), pp. 10–17.

[15] Team, L. L. N. L. C. Scalable linear solvers, hypre 2.0.0. https://computation.llnl.gov/casc/hypre/software.html.

[16] Moin, P., and Apte, S., 2006. "Large-Eddy Simulation of Realistic Gas Turbine-Combustors". *AIAA Journal,* ***44***(4), pp. 698–708.

[17] Apte, S., Martin, M., and Patankar, N., 2009. "A numerical method for fully resolved simulation (FRS) of rigid particle–flow interactions in complex flows". *Journal of Computational Physics,* ***228***(8), pp. 2712–2738.

[18] Apte, S., and Patankar, N., 2007. "A formulation for fully resolved simulation(frs) of particle-turbulence interactions in two-phase flows". *International Journal of Numerical Analysis and Modeling,* ***5***, pp. 1–16.

[19] Calis, H., Nijenhuis, J., Paikert, B., Dautzenberg, F., and Van Den Bleek, C., 2001. "CFD modelling and experimental validation of pressure drop and flow profile in a novel structured catalytic reactor packing". *Chemical Engineering Science,* ***56***(4), pp. 1713–1720.

[20] Nijemeisland, M., and Dixon, A., 2004. "CFD study of fluid flow and wall heat transfer in a fixed bed of spheres". *AIChE journal,* ***50***(5), pp. 906–921.

[21] Magnico, P., 2003. "Hydrodynamic and transport properties of packed beds in small tube-to-sphere diameter ratio: pore scale simulation using an Eulerian and a Lagrangian approach". *Chemical engineering science,* ***58***(22), pp. 5005–5024.

[22] Kuroki, M., Ookawara, S., Street, D., and Ogawa, K., 2007. "High-fidelity CFD modeling of particle-to-fluid heat transfer in packed bed reactors". *ECCE-6, Copenhagen*, pp. 16–21.

[23] Kuroki, M., Ookawara, S., and Ogawa, K., 2009. "A High-Fidelity CFD Model of Methane Steam Reforming in a Packed Bed Reactor". *Journal of Chemical Engineering of Japan,* ***42***(Supplement.), pp. 73–78.

[24] Nelson, B., 2009. "Scaling analysis for the pebble bed of the very high temperature gas-cooled reactor thermal hydraulic test facility". PhD thesis, Oregon State University.

[25] Patankar, N., and Joseph, D., 2001. "Modeling and numerical simulation of particulate flows by the Eulerian–Lagrangian approach". *International Journal of Multiphase Flow,* ***27***(10), pp. 1659–1684.

[26] Patankar, N., Singh, P., Joseph, D., Glowinski, R., and Pan, T., 2000. "A new formulation of the distributed Lagrange multiplier/fictitious domain method for particulate flows". *International Journal of Multiphase Flow,* ***26***(9), pp. 1509–1524.

[27] Patankar, N., 2001. "A formulation for fast computations of rigid particulate flows". *Center for Turbulence Research Annual Research Briefs 2001*, pp. 185–196.

[28] Sharma, N., and Patankar, N., 2005. "A fast computation technique for the direct numerical simulation of rigid particulate flows". *Journal of Computational Physics,* ***205***(2), pp. 439–457.

[29] Gunjal, P., Ranade, V., and Chaudhari, R., 2005. "Computational study of a single-phase flow in packed beds of spheres". *AIChE Journal,* ***51***(2), pp. 365–378.

[30] Johnson, T., and Patel, V., 1999. "Flow past a sphere up to a reynolds number of 300". *Journal of Fluid Mechanics,* ***378***(1), pp. 19–70.

[31] Zhou, J., Adrian, R., Balachandar, S., and Kendall, T., 1999. "Mechanisms for generating coherent packets of hairpin vortices in channel flow". *Journal of Fluid Mechanics,* ***387***(1), pp. 353–396.

[32] Chakraborty, P., Balachandar, S., and Adrian, R., 2005. "On the relationships between local vortex identification schemes". *Journal of Fluid Mechanics,* ***535***(1), pp. 189–214.